



Engineering the electronic structures of hetero-diatomeric iron-manganese sites by d-d orbital hybridization for boosting oxygen reduction

Jun-Kang Li ^a, Fen-Fen Wang ^a, Yang Zhang ^b, Rui Wang ^a, Shu-Na Zhao ^{a,*}, Shuang-Quan Zang ^{a,*}

^a Henan Key Laboratory of Crystalline Molecular Functional Materials, Henan International Joint Laboratory of Tumor Theranostical Cluster Materials, Green Catalysis Center and College of Chemistry, Zhengzhou University, Zhengzhou 450001, PR China

^b School of Materials Science and Engineering, Center of Advanced Analysis & Gene Sequencing, Zhengzhou University, Zhengzhou 450001, PR China



ARTICLE INFO

Keywords:

Atomically dispersed active site
Heteronuclear diatomic catalyst
d-d orbital hybridization
Hollow N-doped carbon nanosphere
Oxygen reduction reaction

ABSTRACT

The catalytic performance of metal single-atom catalysts (SACs) can be further improved through d-d orbital hybridization with adjacent metal sites. However, the construction of metal diatomic catalysts (DACs) remains a great challenge, particularly for heteronuclear DACs. Herein, a heteronuclear DACs with Fe and Mn bimetallic sites embedded on a hollow N-doped carbon nanosphere (HNCS) is successfully achieved through a well-designed two-step anchoring and adsorption method. The obtained Fe/Mn-HNCS catalyst exhibits excellent performance for oxygen reduction reaction (ORR) with a half-wave potential of 0.895 V compared to the single Fe and Mn counterparts. Theoretical calculations reveal that d-d orbital hybridization between Fe-Mn diatomic pair causes a fast electron transfer, optimizes their electronic structures, and reduces the energy barriers for *OH desorption, thereby improving the ORR performance. Our results highlight a simple strategy to synthesize heteronuclear DACs and provide new insights into how diatomic metal sites affect electrocatalytic performance.

1. Introduction

Due to their state-of-the-art catalytic activity, commercial Pt/C catalysts have been widely used for electrocatalytic energy conversion devices, including metal-air batteries and proton exchange membrane fuel cells (PEMFCs) [1–5]. However, their prohibitive cost, low global reserves, and insufficient stability have restricted wide-scale commercialization [6,7]. Therefore, developing cost-effective, efficient, and durable electrocatalysts with earth-abundant elements is of great importance to accelerate the large-scale application of this clean energy conversion technology, thus upgrading the present energy technology landscape [8–10].

Recently, metal single-atom catalysts (SACs) embedded in N-doped carbon (NC) matrix have exhibited encouraging activity and stability for the ORR in metal-air batteries and PEMFCs, possessing great promise to replace commercial Pt/C catalysts [11–14]. The ORR electrocatalytic performance of SACs is usually determined by the coordination microenvironment of single MN_x sites, the loading amount of metal, the structure of NC matrix, and the metal-support interaction [15–22]. Modulation of the coordination microenvironment of active MN_x sites is the most common way to further improve the ORR performance of SACs materials by reducing energy barriers of oxygenated intermediates

adsorption/desorption at MN_x sites [23–26]. Many recent works have demonstrated that the adjacent metal nanoparticles (NPs) can modulate the geometric and electronic structure of single MN_x active sites, resulting in excellent ORR performance [26,27]. The coordination number of single metal centers also showed a noticeable effect on ORR performance [28,29]. For example, the most recent work reported by Sun and coworkers demonstrated that the ORR performance of FeN₄ sites could be modulated by the axial ligands by tailoring the energy gap between the Fe 3d_z² and OH p_{xpy} [30]. Thus, PFePc with a weak-field axial ligand I had the lowest Fe 3d_z² orbital energy level, exhibiting superior ORR activity in alkaline electrolytes. Changing coordinated atom species of single metal centers by partially replacing coordinated N atoms with other nonmetallic atoms (B, P, and S, etc.) is a useful way to improve the ORR activity [31,32]. Because of their discrepancy in atomic radius, electron spin density, and electronegativity, the local electronic properties of the active metal centers can be optimized by the p-d orbital hybridization, thus boosting ORR catalytic performance. Interestingly, the new emerging DACs (especially for the heteronuclear DACs) showed a strong synergistic effect in diatomic active sites to lower the reaction barrier and accelerate the reaction kinetics by the d-d electronic interaction between adjacent isolated metal sites [33–40]. A planar-like Fe₂N₆ configuration exhibited a unique redox transition of

* Corresponding authors.

E-mail addresses: zhaosn@zzu.edu.cn (S.-N. Zhao), zangsqzg@zzu.edu.cn (S.-Q. Zang).

ORR from $O_x\text{-Fe}^{3+}\text{-Fe}^{2+}$ to $\text{Fe}^{2+}\text{-Fe}^{2+}$, which triggered a strong driving force for the break of the O–O bond [36]. Therefore, it can accelerate the ORR catalytic kinetics and has seen more than 700% increase in mass activity than the FeN_4 sites. Interestingly, a bifunctional DACs with Ni–Fe heteronuclear pairs displayed excellent electrocatalytic performance and stability for both ORR and oxygen evolution reaction (OER) [37]. Such superior catalytic activity is attributed to the orbital coupling between Ni atom and Fe atom in the heteronuclear pairs, therefore leading to a higher oxidation state of Fe and optimization of the binding strength with the reaction intermediates both for ORR and OER. However, the current method of pyrolysis, which directly pyrolyzed the mixture of hetero-metal ions and carbon substrates, generally leads to the low proportion of heteronuclear pairs or to the formation of undesired metal NP species. The use of hetero-metal dimer molecules as heterometallic sources offers a promising way to construct heteronuclear DACs. But the limited precursors of heterometallic dimers, their complex synthetic processes, and their undesired thermal migration under pyrolysis conditions seriously hamper the broad application of this method. In addition, the structure of NC matrices is always out of control during the pyrolysis process, which prevents the study of the nature of heteronuclear pairs in the ORR. Therefore, the rational construction of homo- and heteronuclear DACs with the same NC structures is still a big challenge.

Herein, a heteronuclear DACs with Fe and Mn bimetallic sites embedded on a hollow N-doped carbon nanosphere (HNCS) is successfully achieved through a well-designed two-step anchoring and adsorption method. Firstly, the Fe-HNCS catalyst with single Fe sites is synthesized with SiO_2 spheres as hard templates. This HNCS matrix with a thin and loose carbon shell is beneficial for the fast mass transport of O_2 during the catalytic reactions. Next, the Mn atom is introduced and followed by a second pyrolysis process. This two-step method not only increases the metal loading, but also facilitates the formation of heteronuclear Fe–Mn pairs by catching Mn close to the Fe sites on the Fe-HNCS. The Fe–Mn pairs are characterized by aberration-corrected scanning transmission electron microscopy (AC-STEM) and X-ray absorption spectroscopy (XAS) analysis. Due to the unique dual Fe–Mn configuration, the Fe/Mn-HNCS exhibits excellent ORR activity with an onset potential (E_{onset}) of 1.13 V and a half-wave potential ($E_{1/2}$) of 0.895 V compared to the single atom Fe and Mn catalysts. Theoretical calculations demonstrated that the Fe atom in the Fe–Mn pair is more active for the ORR in Fe/Mn-HNCS, while the existence of an adjacent Mn atom plays an important role in the engineering of the electronic structures of the Fe site through d–d orbital hybridization. Further investigation by the crystal orbital Hamilton population (COHP) and Bader charge analysis disclosed that the optimized d orbital structure of the Fe site in Fe/Mn-HNCS weakens the over-strong adsorption of $^*\text{OH}$, thus resulting in outstanding ORR activity. Our results highlight a simple strategy to synthesize heteronuclear DACs and provide new insights into how diatomic metal sites affect electrocatalytic performance.

2. Experimental section

2.1. Materials

All reagents were obtained from commercial sources and used as received without further purification. (3-aminopropyl)triethoxysilane (99%), tetraethyl orthosilicate (99%), 5,10,15,20-Tetrakis(4-amino-phenyl)-21H,23H-porphine (TAPP, 95%), 2,2'-bipyridine-5,5'-dicarbox-aldehyde (BPDA, 98%), Iron (II) chloride anhydrous (FeCl_2 , 99.5%), ammonium chloride (99.5%), were obtained from Sinopharm Chemical.

2.2. Preparation of the HNCS and Fe/Mn-HNCS electrocatalyst

Synthesis of HNCS: 120.0 mg of $\text{SiO}_2\text{-CHO}$ was ultrasonically dispersed in 1.6 mL of n-butanol and 1.8 mL of 1,2-dichlorobenzene, then 20.0 mg of TAPP was added to the above mixture and stirred for

0.5 h, and finally 16.0 mg of BPDA and 0.215 mL of 6.0 M acetic acid were added. The mixture was transferred to the autoclave and reacted in an oven at 120 °C for 48 h. After the product was filtered, the filter cake was washed three times with 1,4-dioxane and acetone, then dried under vacuum for 12 h. The solid powder was placed in a crucible and calcined up to 800 °C kept for 3 h under N_2 atmosphere with a ramping rate of 5 °C min⁻¹. Finally, SiO_2 was etched with 6.0 M NaOH, washed with water, and then dried to obtain HNCS.

Synthesis of Fe/Mn-HNCS: 30.0 mg of Fe-HNCS, 1.3 mg of manganese acetate, and 300.0 mg of ammonium chloride were ground by mortar and pestle. Then, the obtained composite was annealed at 800 °C and maintained for 2 h under a N_2 flow, and the ramping rate is 5 °C min⁻¹ to yield Fe/Mn-HNCS.

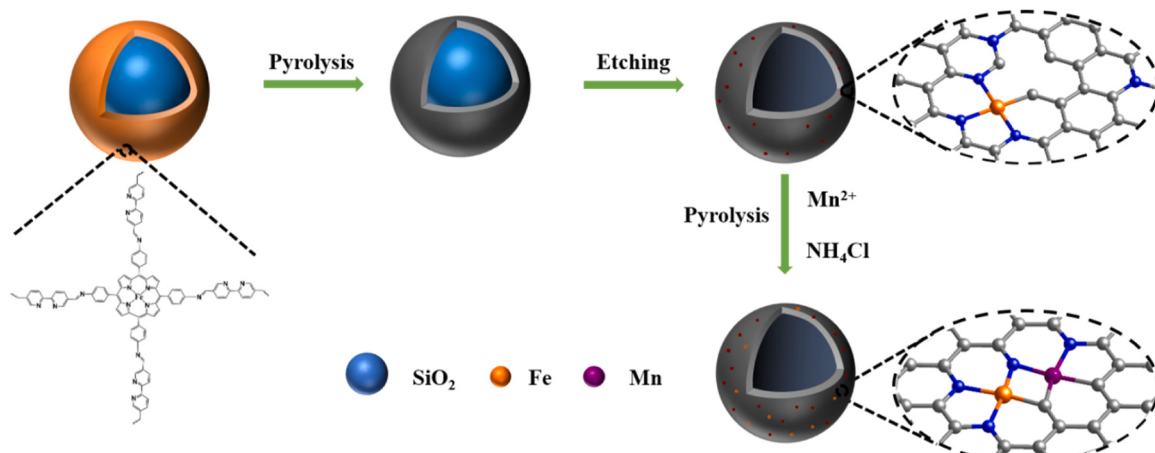
More experimental details can be found in Supporting Information.

3. Results and discussion

3.1. Synthesis and characterization of Fe/Mn-HNCS

The preparation route of Fe/Mn-HNCS was schematically illustrated in Scheme 1. In order to synthesize electrocatalysts with the HNCS structure, SiO_2 spheres with uniform sizes were chosen as the templates (Fig. S1). A Fe-porphyrin complex with single Fe sites was chosen as the precursor of Fe, C, and N, which was coated on the SiO_2 spheres through imine condensation with the BPDA ligand to form a core-shell $\text{SiO}_2@\text{POP}$ nanosphere (POP = porous organic polymer). The POP helps the separation of the Fe-porphyrin complexes by the BPDA ligands, which is beneficial for metal dispersion. The as-prepared $\text{SiO}_2@\text{POP}$ was then thermally treated under N_2 atmosphere to form a $\text{SiO}_2@\text{NC}$ nanosphere (Fig. S2) and followed by etching the SiO_2 cores in a NaOH solution. By carefully controlling the amount of the Fe-porphyrin complex, Fe-HNCS with single Fe sites embedded in the hollow nanosphere can be successfully obtained (Fig. S3). The single Fe sites are confined by the strong Fe–N bonds, which limits the diffusion of Fe atoms in the second pyrolysis process. Meanwhile, doping Fe atom in the first step can reduce the release of N species, providing more N-coordination sites for the subsequent adsorption of metal ions. An ion adsorption followed by a second pyrolysis process was then conducted to increase the density of the active Mn_x sites using Fe-HNCS as the host. Furthermore, the N atoms are relatively enriched around the Fe atoms in the Fe-HNCS matrix, making it an ideal host to prepare DACs. Additionally, the ammonium chloride (NH_4Cl) can release NH_3 and HCl under the pyrolysis process at high temperature, which could be used as a foaming agent to create an abundant porous structure in the HNCS matrix [41]. Besides, it not only provides additional nitrogen sources (NH_3) for anchoring Fe and/or Mn, but also helps the dispersion of Fe and/or Mn in the HNCS matrix. Thus, Fe/Mn-, Mn/Mn-, and Fe/Fe-HNCS with hollow nanospherical structures and increased density of active sites were prepared by a two-step anchoring and adsorption method, conforming by higher metal content determined by ICP-OES (Table S1). In comparison, Fe-NC was obtained by thermal decomposition without the SiO_2 template.

The morphology and microstructure of the as-synthesized Fe/Mn-HNCS are firstly characterized by advanced electron microscopy techniques. The image contrast of high-angle annular dark-field scanning transmission electron microscopy (HAADF-STEM) strongly depends on the atomic number, varying approximately as Z^2 for isolated atoms [38]. Therefore, HAADF-STEM imaging is widely used to study SACs with the features of directly interpretable in terms of crystal structure and chemical information [42]. As presented in Fig. 1a, b and S4a, b, The Fe/Mn-HNCS displays a spherical structure with the original morphology and size of the SiO_2 templates. It's difficult to study the distribution of small nanoparticles merely from 2 dimensions imaging; electron tomography was used to reliably assess the existence of nanoparticles and integrity of the shell in 3 dimensions (3D). It can be observed that the HNCS have a quasi-spherical morphology without aggregations of nanoparticles from the 3D reconstructions results as



Scheme 1. Schematic illustration of synthetic procedure for Fe/Mn-HNCS.

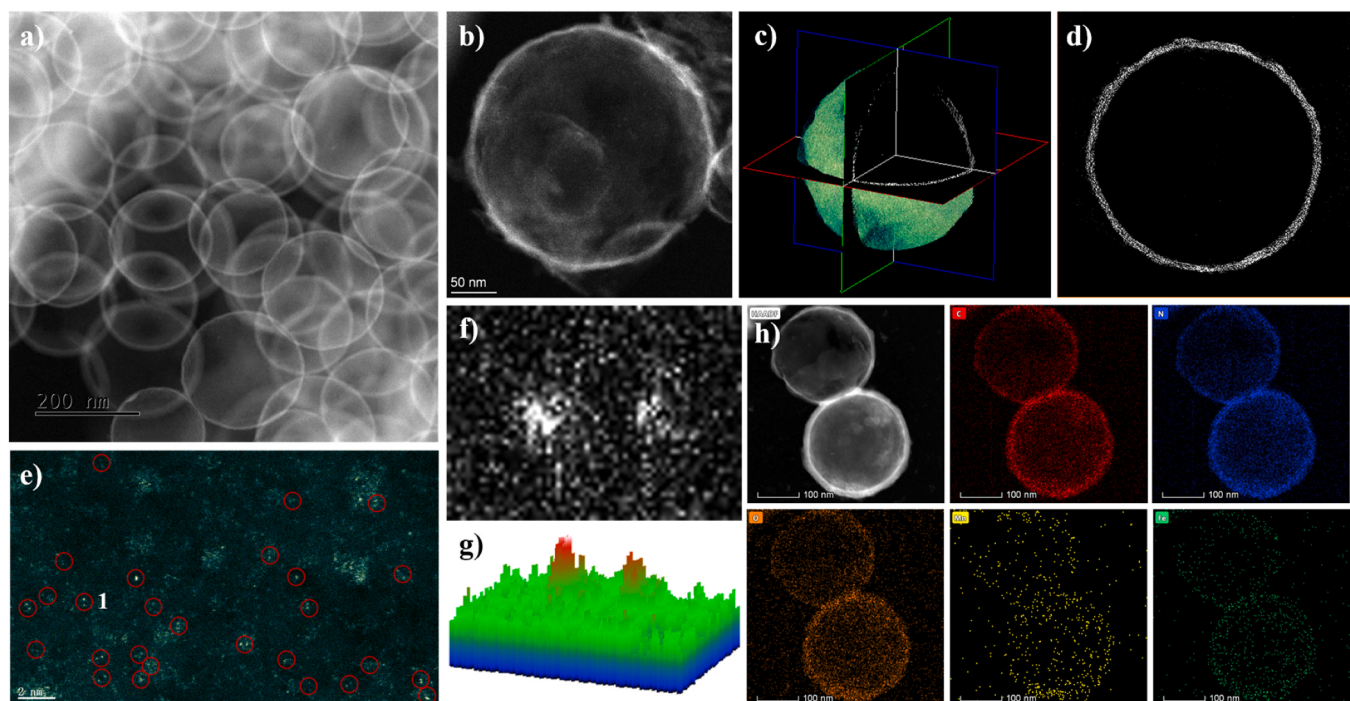


Fig. 1. Morphological characterization of Fe/Mn-HNCS: (a,b) HAADF-STEM images. (c) Electron tomography reconstruction of a typical nanoparticle. The 3D volume rendering image indicated that the sample is hollow inside. (d) The slices through the 3D reconstructions proved the hollow structure inside and the loose voids in the shell structure. (e) High-resolution HAADF-STEM image. (f) Magnified image of the selected Fe-Mn DAC at position 1 along the $X_{\max}-X_{\min}$ direction in (e). (g) The 3D intensity profile of position 1. (h) Corresponding element mappings.

shown in the Movies M1 and M2, indicating the atomic dispersion of Fe and Mn atoms. Surface visualizations clearly indicate the presence of a void in the core as shown in Fig. 1c and 1d, furthermore, the shell is ~ 10 nm with a loose structure which is beneficial for the O_2 diffusion and fast mass transport during the catalysis reactions (Fig. S4c). By further zooming in the HAADF-STEM image, many bright spots can be detected on the thin carbon shell, further confirming the formation of isolated single Fe and Mn atoms (Fig. 1e). Besides, the atomic pair structure appears as highlighted by the red circle (Fig. 1e-g). Through statistical analysis over multiple atomic pairs, the average dimer distance is ~ 2.6 Å, indicating the possible formation of metal-metal bonds [43,44]. For comparison, Mn/Mn- and Fe/Fe-HNCS samples were also prepared in the same procedure. The high-resolution HAADF-STEM images of Mn/Mn- and Fe/Fe-HNCS samples confirm the existence of isolated Fe or Mn atoms homogeneously dispersed on the thin carbon

shell, whereas neither atomic Mn_2 pairs nor Fe_2 pairs can be detected (Fig. S5a,b and S6a,b). The above results indicate that Mn atoms are inclined to anchor on the neighbor of isolated single Fe sites in Fe-HNCS, resulting in the formation of Fe-Mn bimetallic pairs. The energy-dispersive X-ray spectroscopy (EDS) mappings results of Fe/Mn-, Mn/Mn-, and Fe/Fe-HNCS reveal that the Fe and Mn atoms are highly dispersed over the entire carbon shell (Fig. 1h, S5c and S6c). In contrast, obvious aggregation of Fe was observed in Fe-NC, demonstrating the SiO_2 templates benefit the dispersion of Fe atoms during the pyrolysis process (Fig. S7).

Supplementary material related to this article can be found online at doi:10.1016/j.apcatb.2023.123090.

Supplementary material related to this article can be found online at doi:10.1016/j.apcatb.2023.123090.

Powder X-ray diffraction (PXRD) was also performed to analyze the

phase composition of the as-prepared samples (Fig. S8). All the samples show a broad peak at around 26° , which can be assigned to the (002) plane of graphitic carbon, indicating the good degree of graphitization of the HNCS matrix. No characteristic peak associated with metal NPs species can be detected in the XRD patterns of Fe/Mn-, Mn/Mn-, and Fe/Fe-HNCS samples, suggesting the high dispersion of Fe and Mn species. However, obvious Fe and Fe₄N species can be observed in the patterns of Fe-NC, which is in agreement with the STEM results. Raman measurements were then performed to characterize the disorders/defects of the HNCS matrix. The Raman spectra of the as-prepared samples show two prominent peaks at about 1340 cm^{-1} and 1590 cm^{-1} , corresponding to the disordered carbon atoms at the edges and defect sites with A_{1g} symmetry (D band) and well-ordered graphitic carbon atoms with E_{2g} symmetry (G band), respectively (Fig. S9) [45]. Generally, the high intensity ratio (I_D/I_G) of D band and G band could reflect abundant disordered/defects in HNCS matrix. The Raman spectra exhibit that the I_D/I_G ratios of HNCS increase after loading Fe and/or Mn, indicating that introducing Fe and/or Mn can create more defect sites in the HNCS matrix. In addition, Fe/Mn-HNCS displays an even higher I_D/I_G ratio (1.35) than that of Mn/Mn- (1.24) and Fe/Fe-HNCS (1.29), which suggests the further increase in defect sites and disorder is caused by heterometal Fe and Mn doping. The porous feature of the as-prepared samples was analyzed by the N_2 adsorption-desorption isotherms. The isotherms of the as-prepared samples display hysteresis loops in relative pressure of 0.4–1.0 and an abruptly increased N_2 adsorption at low

relative pressure, revealing the co-existence of micro- and mesopores (Fig. S10 and Table S2). The pore size distribution curves of the as-prepared samples analyzed by non-local density functional theory (NL-DFT) showed that the micropores are the major part (Fig. S11). Fe/Mn-HNCS shows a large Brunauer-Emmett-Teller (BET) surface area ($665.4\text{ m}^2\text{ g}^{-1}$) with a total pore volume of $1.25\text{ cm}^3\text{ g}^{-1}$, which is slightly higher than those of Mn/Mn-HNCS ($615.7\text{ m}^2\text{ g}^{-1}$ and $0.97\text{ cm}^3\text{ g}^{-1}$) and Fe/Fe-HNCS ($604.6\text{ m}^2\text{ g}^{-1}$ and $0.89\text{ cm}^3\text{ g}^{-1}$) as well as much higher than that of HNCS ($332.2\text{ m}^2\text{ g}^{-1}$ and $0.70\text{ cm}^3\text{ g}^{-1}$). These results demonstrate that Fe and/or Mn doping improves the porosity during the pyrolysis process, which favors the exposure of isolated catalytic sites and accelerates O_2 diffusion and mass transport in ORR.

The surface elemental compositions and electronic states were revealed by X-ray photoelectron spectroscopy (XPS) and XAS measurements. The high-resolution N 1s XPS spectra of the as-prepared samples show that N mainly existed as pyridinic N (398.6 eV), graphitic N (400.8 eV), and some oxidized N (403.4 eV) (Fig. S12). Generally, the pyridinic N can anchor metal sites and decrease the overpotential of ORR. Additionally, graphitized N has good conductivity, thus promoting electron transfer during the ORR process [46]. To further investigate the local atomic configuration of Fe and Mn atoms, the X-ray absorption near-edge structure (XANES) and extended X-ray absorption fine structure (EXAFS) measurements were conducted for the Fe/Mn-, Mn/Mn-, and Fe/Fe-HNCS samples. Fig. 2a displays the XANES spectra of Fe K-edge for Fe/Mn- and Fe/Fe-HNCS as well as those of the Fe foil,

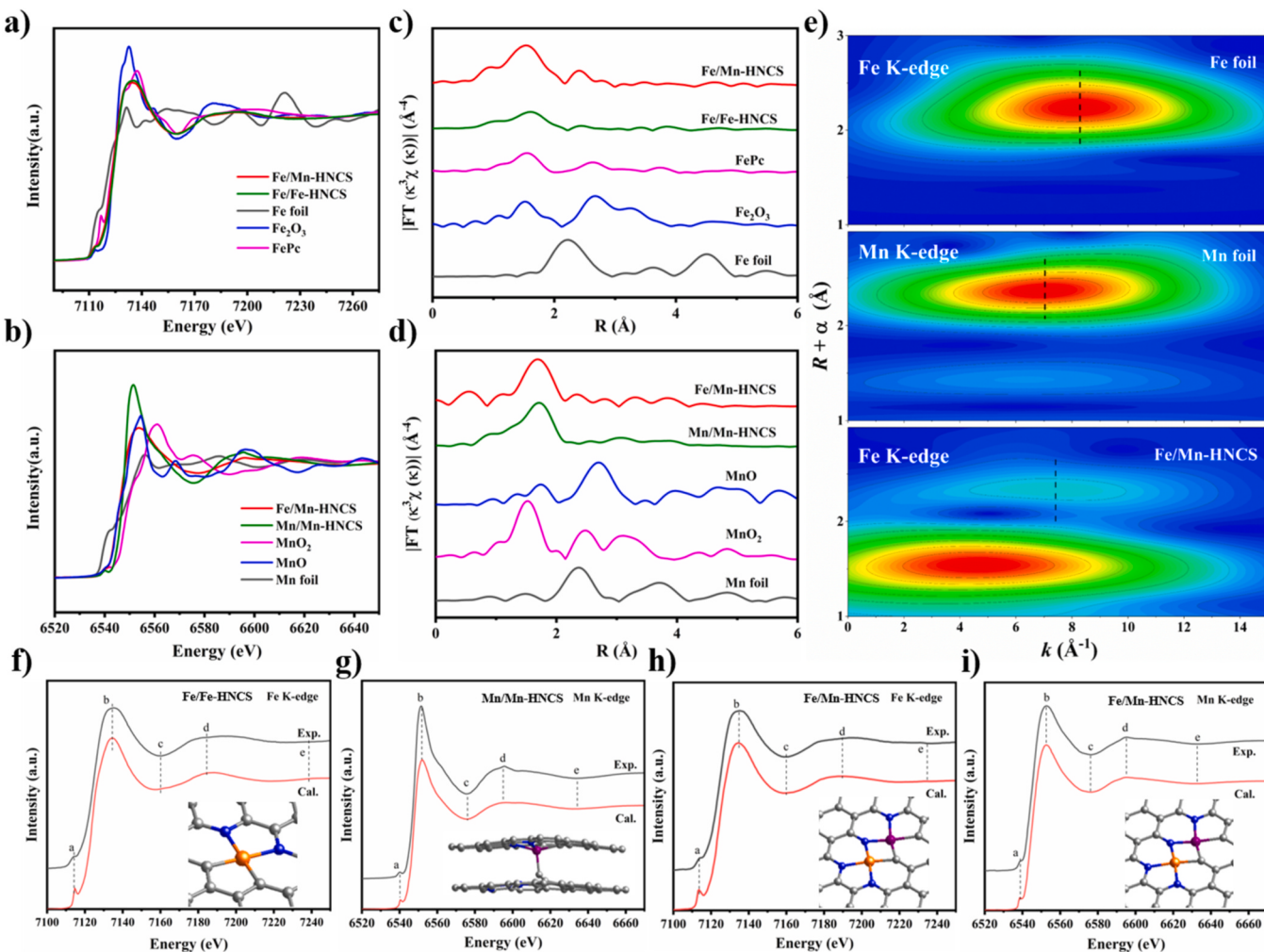


Fig. 2. (a) Fe K-edge XANES and (b) Mn K-edge XANES spectra of Fe/Mn-, Mn/Mn-, Fe/Fe-HNCS, and reference samples. (c,d) FT-EXAFS spectra of Fe/Mn-, Mn/Mn-, Fe/Fe-HNCS, and reference samples. (e) WT-EXAFS plots of Fe foil, Mn foil, and Fe K-edge of Fe/Mn-HNCS. Comparison between the K-edge XANES experimental spectra of Fe/Fe-HNCS (f), Mn/Mn-HNCS (g) and Fe/Mn-HNCS (h,i) and the theoretical spectra calculated with the depicted structures.

FePc and Fe₂O₃ benchmarks. The K-edge position of Fe in both Fe/Mn- and Fe/Fe-HNCS sits between those of FePc and Fe₂O₃, implying that the average valence state of Fe in Fe/Mn- and Fe/Fe-HNCS is between +2 and +3. The oxidation state of Fe in Fe/Fe- and Fe/Mn-HNCS samples were qualitatively determined by the fitting curves. The Fe valence state in Fe/Mn-HNCS is estimated to be +2.3, which is slightly lower than the average Fe valence state in Fe/Fe-HNCS (+2.4) (Fig. S13a). Similarly, the Mn K-edge positions in Fe/Mn- and Mn/Mn-HNCS are situated between those of MnO and MnO₂, revealing the positive charge of the Mn center of both Fe/Mn- and Mn/Mn-HNCS samples (Fig. 2b). The average Mn valence state in Fe/Mn- and Fe/Fe-HNCS samples are estimated to be 2.0 and 2.4, respectively (Fig. S13b).

Moreover, the local coordinated environment of Fe or Mn is monitored by Fourier transform (FT) of k^3 -weighted EXAFS results. The EXAFS spectra of Fe K-edge in both Fe/Mn- and Fe/Fe-HNCS feature a distinguished peak at $\sim 1.5 \text{ \AA}$, which arises from a Fe-C/N scattering path with the calculated coordination number (CN) of ~ 4 (Fig. 2c and Table S3). Similarly, a dominant peak at $\sim 1.6 \text{ \AA}$ in the EXAFS spectra collected at Mn K-edge of both Fe/Mn- and Mn/Mn-HNCS could be ascribed to the Mn-C/N scattering path (Fig. 2d). Interestingly, the calculated CN of Mn-C/N coordination in Mn/Mn-HNCS is ~ 5 , which is different from that in Fe/Mn-HNCS ($\text{CN}_{\text{Mn-C/N}} = \sim 4$) (Table S4). The fifth CN of M-C/N coordination in SAC catalysts is usually in the axial direction, which also can optimize the electronic structure of the isolated M center and thus enhance the ORR catalytic activity [30]. It is worth noting that the typical peaks derived from Fe-Fe coordination (at $\sim 2.2 \text{ \AA}$) and Mn-Mn coordination (at $\sim 2.3 \text{ \AA}$) are not detected, revealing that Fe and Mn species in the M/M-HNCS samples show atomic-level dispersion. Importantly, a new metal-metal path located at $\sim 2.4 \text{ \AA}$ appears in Fe/Mn-HNCS, confirming the formation of Fe-metal diatomic configuration. The calculated CN of the Fe-metal diatomic feature is about 0.6 (Table S3), revealing the coexistence of isolated Fe and Mn sites as well as Fe-metal pairs, which is consistent with the HAADF-STEM results. According to the fitting result from EXAFS results, the Fe atoms in Fe/Mn- and Fe/Fe-HNCS fitted well with FeN₃C and FeN₂C₂ structure, whereas, Mn atoms in Fe/Mn- and Mn/Mn-HNCS fitted well with MnN₂C₂ and MnN₂C₃ (Fig. S14). Wavelet transform (WT) analysis with high resolution in both k and R space, which is capable of distinguishing lighter and heavier backscattering atoms, could further discriminate different coordination structures [47]. As illustrated in Fig. S15, the WT intensity maximum of around 5 \AA for the Fe/Mn-, Mn/Mn-, and Fe/Fe-HNCS samples originates from the coordination with the light atoms, which can assign to Fe-C/N or Mn-C/N bonding. Meanwhile, no WT signals from Fe-Fe bond (8.2 \AA^{-1}) and Mn-Mn bond (6.9 \AA^{-1}) are observed, further confirming the atomic dispersion of Fe and Mn species in the HNCS matrix. Remarkably, the WT signal of Fe-metal pair in Fe K-edge of Fe/Mn-HNCS is at 7.4 \AA , which is located between Fe-Fe bond and Mn-Mn bond, strongly proving the formation of Fe-Mn heterometallic pair (Fig. 2e). However, the Fe-Mn feature in Mn K-edge is not detected, mainly because the different modes of atomic vibration may result in differences in signal intensity [48]. Since the XANES spectra are more sensitive to the atomic configuration of the MN_x moiety, XANES simulation calculations were conducted. The simulated XANES spectra of the FeN₂C₂-1 and MnN₂C₃-1 models well mimicked the experimental profiles, suggesting that FeN₂C₂-1 and MnN₂C₃-1 models are the most possible structures for Fe/Fe- and Mn/Mn-HNCS, respectively (Figs. 2f, 2g and S16). The theoretical spectrum of the Mn K-edge in the FeN₃C-Mn-1 model is matched well with the main experimental features (Fig. 2i and S16). In addition, the calculated XANES spectra of the Fe K-edge in the FeN₃C-Mn-1 model reproduced all the features for the experimental spectra better than the FeN₃C-Fe-1 model (Fig. 2h, S16 and S17). These XANES simulations further confirm that the existence of Fe-Mn pairs in Fe/Mn-HNCS.

3.2. Catalytic ORR and Zn-air battery performances of electrocatalysts

The electrocatalytic ORR performance of as-prepared samples was evaluated by cyclic voltammetry (CV) and linear sweep voltammetry (LSV) via rotating disk electrode (RDE) technique. HNCS and Fe-NC samples were also tested under the same conditions to evaluate the importance of the metal center and the hollow structure. All potentials were referenced to the Reversible Hydrogen Electrode (RHE). As revealed in Fig. S18, the CV curves of the as-prepared samples in a N₂-saturated solution are devoid of any feature peaks, whereas a clear cathodic reduction peak appeared for all the samples in the O₂-saturated case, reflecting their ORR catalytic activity. The metal-free HNCS sample displayed poor electrocatalytic ORR performance from the LSV results with E_{onset} at 0.895 V and $E_{1/2}$ at 0.74 V (Fig. 3a,b). The $E_{1/2}$ of Fe-HNCS and Mn-HNCS is improved significantly, which is 40 mV and 110 mV positively shifted than that of HNCS, indicating the key role of single metal sites for ORR activity. After anchoring metal ions in the second step, Fe/Fe- and Mn/Mn-HNCS samples show improved ORR performance with $E_{1/2}$ of 0.84 V and 0.875 V respectively, owing to the increasing number of active single metal centers. More interestingly, although Fe/Mn-HNCS had similar metal loading to Fe/Fe- and Mn/Mn-HNCS samples, it exhibits the highest ORR activity with E_{onset} of 1.13 V, $E_{1/2}$ of 0.895 V as well as limiting current density (J_L) of 5.67 mA cm⁻², outperforming that of commercial Pt/C catalysts (Fig. 3a,b). This remarkable improvement in ORR performance is primarily attributed to the synergistic effect of neighboring Fe and Mn dual active sites. In addition, Fe/Mn-HNCS displays a high kinetic current density (J_K) of 15.53 mA cm⁻² at 0.85 V, which is almost 3 times higher than that of commercial Pt/C, further revealing the excellent ORR performance of Fe/Mn-HNCS. As a comparison, the Fe-NC sample without a hollow structure shows the worst ORR performance among all the samples, indicating the importance of the hollow structure for the ORR activity.

The ORR catalytic pathway of the as-prepared samples was further clarified through the RDE measurements at different rotating rates (from 400 to 2500 rpm) (Fig. S19). The linearity of the Koutecky-Levich (K-L) plots for the as-prepared samples suggests a first-order reaction kinetic for ORR. The electron transfer number (n) of Fe/Mn-, Mn/Mn-, and Fe/Fe-HNCS is calculated to be close to the theoretical value of 4 from the K-L plots, indicating the desired 4e⁻ ORR process towards the formation of H₂O. While the n of HNCS is about 3, suggesting the coexistence of the 2e⁻ and 4e⁻ pathways, which can be used to explain the poor ORR performance of HNCS. Besides, the smallest Tafel slope of 69.8 mV dec⁻¹ is observed for Fe/Mn-HNCS as compared with those of Mn/Mn- and Fe/Fe-HNCS, implying its fast reaction kinetics for the ORR process due to the synergistic effect of Fe and Mn dual active sites (Fig. 3c). Moreover, electrochemical impedance spectroscopy (EIS) measurements disclose that Fe/Mn-HNCS had the lowest charge transfer resistance during the electrocatalytic ORR process than other samples, further revealing its advantage in the catalytic dynamic (Fig. S20). To further get an in-depth understanding of the intrinsic activity of the as-prepared samples, electrochemical surface area (ECSA) was then indirectly evaluated by the electrochemical double layer capacitance (C_{dl}) (Fig. S21). As illustrated in Fig. 3d, the C_{dl} of Fe/Mn-, Mn/Mn-, and Fe/Fe-HNCS is almost 2 times higher than that of the Fe-NC sample, suggesting that the hollow structure provides more exposed active sites. Interestingly, Fe/Mn-HNCS processed larger C_{dl} (40.0 mF cm⁻²) than Mn/Mn- (30.9 mF cm⁻²) and Fe/Fe-HNCS (27.8 mF cm⁻²). Thus, it can be deduced that introducing hetero-metal in the hollow structure can make more defects and further increase the surface area, thus enlarging the ECSA. Therefore, Fe/Mn-HNCS can provide more accessible active sites and facilitate the ORR performance.

The long-term durability and methanol tolerance are also crucial parameters to evaluate the activity of ORR electrocatalysts in practical applications. As illustrated in Fig. S22a, $E_{1/2}$ of Fe/Mn-HNCS was almost unchanged after operation for 5000 cycles. The longer stability of Fe/Mn-HNCS were evaluated by LSV cycling for 10000 cycles (Fig. S23).

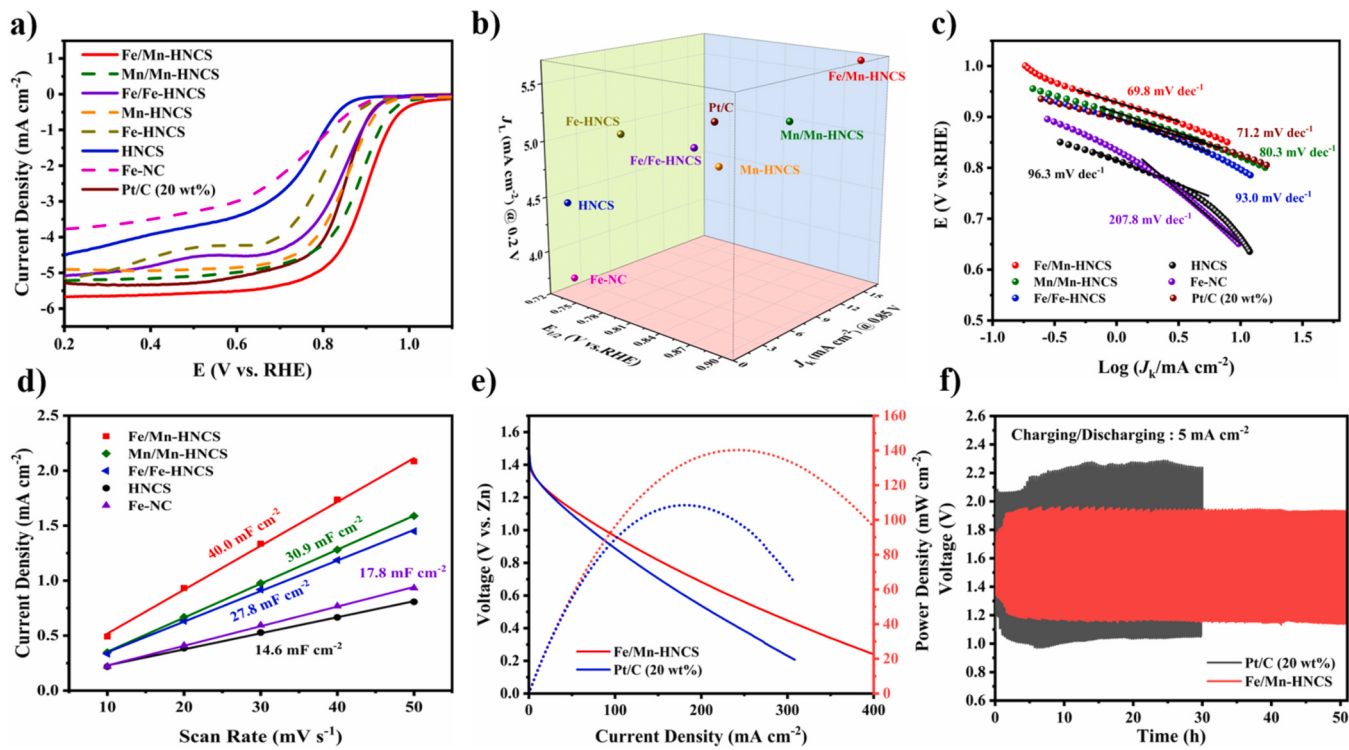


Fig. 3. (a) ORR polarization curves of the as-prepared samples and Pt/C catalyst. (b) Comparisons of J_L , J_K , and $E_{1/2}$ of the as-prepared samples and Pt/C catalyst. Corresponding Tafel plots derived from the LSV curves. (d) Linear fitting of capacitive currents of the as-prepared samples vs. scan rate. (e) Polarization and power density plots of Fe/Mn-HNCS and Pt/C electrocatalysts. (f) Charge-discharge curves of Fe/Mn-HNCS and Pt/C electrocatalysts at 5 mA cm^{-2} .

The $E_{1/2}$ of Fe/Mn-HNCS was 17 mV negative shift after 10000 cycles, while that of Pt/C showed similar negative shift after 5000 cycles (Fig. S22b), demonstrating the excellent stability of Fe/Mn-HNCS during ORR process. A chronoamperometric test was also carried out to further corroborate the magnificent electrochemical stability of Fe/Mn-HNCS. About 87.5 % of original current density was retained for Fe/Mn-HNCS after running the ORR reaction for 20 000 s, whereas Pt/C only showed 81.1 % of current retention under the same conditions (Fig. S22c). Although the PXRD pattern of the used Fe/Mn-HNCS does not change, some isolated Fe and Mn atoms aggregate into clusters after long-time electrolysis, resulting in the ORR instability (Fig. S24). Moreover, negligible ORR current change was observed for Fe/Mn-HNCS compared with Pt/C after the injection of 5 mL methanol into 0.1 M KOH electrolyte, revealing its strong tolerance to methanol crossover (Fig. S22d). To confirm the crucial role of isolated Fe/Mn sites for the superior ORR performance, the SCN⁻ poison experiment was also performed to block the isolated Fe/Mn sites. Upon the addition of SCN⁻ into ORR system of Fe/Mn-HNCS, the $E_{1/2}$ and J_L both showed significantly decreased of 25 mV and 0.44 mA cm^{-2} respectively, clearly revealing that isolated Fe/Mn sites constitute the key active centers for ORR (Fig. S25).

Based on the outstanding ORR performance of Fe/Mn-HNCS, a homemade Zn-air battery (ZAB) is assembled in this work (Fig. S26a). As anticipated, the homemade ZAB with Fe/Mn-HNCS as the air cathode showed a high open-circuit voltage (≈ 1.45 V) and a large peak power density of 140.3 mW cm^{-2} at 239.0 mA cm^{-2} , which considerably exceeded 108.5 mW cm^{-2} of commercial Pt/C (Fig. 3e and Fig. S26b). Moreover, the excellent long-term stability is illustrated by over 50 h at 5 mA cm^{-2} , where the voltage gap barely changes (Fig. 3f). As shown in Fig. S26c, a red-emitting diode (2.0 V) could be lighted up by two Fe/Mn-HNCS-based ZABs in series. These results revealed the great potential of Fe/Mn-HNCS as an air cathode in practical applications.

3.3. Mechanism analysis

To further provide an in-depth understanding of the superior ORR catalytic performance of Fe/Mn-HNCS, density functional theory (DFT) calculations were conducted. According to the fitting result from EXAFS results, the Fe and Mn atom in the Fe/Mn-HNCS fitted well with FeN₃C and MnN₂C₂ structures, respectively. Therefore, there are three possible models in the Fe-Mn pairs, that is FeN₃C-Mn-1, FeN₃C-Mn-2, FeN₃C-Mn-3 (Fig. S16). The formation energies were computed to investigate the thermodynamic stability of these models (Table S5). The FeN₃C-Mn-1 (-9.0064 eV) shows much more negative formation energy than those of FeN₃C-Mn-2 (-6.3358 eV) and FeN₃C-Mn-3 (-6.8167 eV), revealing that the FeN₃C-Mn-1 model is more stable in thermodynamics. To further analyze the structural stability of these models, projected COHP (pCOHP) and integrated COHP (ICOHP) were also performed to evaluate the interaction between the Fe/Mn centers and nitrogen atoms (Fig. S27). Quantitatively, the integrated bonding strength of Fe-N and Mn-N of the FeN₃C-Mn-1 model were calculated to be -0.68 eV and -0.63 eV respectively, which is negative than those of the FeN₃C-Mn-2 (-0.33 eV for FeN₃C site and -0.37 eV for MnN₂C₂ site) and FeN₃C-Mn-3 models (-0.53 eV for FeN₃C site and -0.52 eV for MnN₂C₂ site), resulting in the strong binding strength of Fe-N and Mn-N bonds in FeN₃C-Mn-1 model. Therefore, the FeN₃C-Mn-1 model is more stable than FeN₃C-Mn-2 and FeN₃C-Mn-3 models. Other representative structures, including Fe-Fe diatomic sites, FeN₃C sites, FeN₂C₂ sites, and MnN₂C₃ sites were also prepared (Fig. S16). Although FeN₃C-Fe-1 (-8.9282 eV) show similar formation energy to the FeN₃C-Mn-1 (-9.0064 eV), the integrated bonding strength of Fe-N and Mn-N in FeN₃C-Mn-1 model (-0.68 eV and -0.63 eV respectively) is stronger than that in FeN₃C-Fe-1 model (-0.62 eV) (Fig. S27). Thus, FeN₃C-Mn-1 model is more stable in thermodynamics. Furthermore, considering the above-mentioned result of XANES simulations and WT analysis, FeN₃C-Mn-1 is the most possible existed structure in Fe/Mn-HNCS.

Then, the Gibbs free energy diagrams for ORR on FeN₃C site and

MnN_2C_2 site in $\text{FeN}_3\text{C}-\text{Mn-1}$, $\text{FeN}_2\text{C}_2-\text{1}$, $\text{MnN}_2\text{C}_3-\text{1}$ and $\text{Pt}(111)$ were calculated at the potential of $U = 0 \text{ V}$ (Fig. 4a and S28). As shown in Fig. 4a, the step of $^*\text{OH}$ desorption in $\text{FeN}_2\text{C}_2-\text{1}$ site is endothermic with a large limiting-potential of 1.49 V . Thus, the ORR performance of $\text{FeN}_2\text{C}_2-\text{1}$ is restricted by $^*\text{OH}$ reduction to H_2O , due to the over strong adsorption of $^*\text{OH}$ on Fe atom. While, all four elementary steps of the ORR process on FeN_3C and MnN_2C_2 sites in $\text{FeN}_3\text{C}-\text{Mn-1}$, $\text{MnN}_2\text{C}_3-\text{1}$ sites, and $\text{Pt}(111)$ are consistent downhill at $U = 0 \text{ V}$, implying a spontaneous exothermal process (Fig. 4a). The rate determining step (RDS) of both FeN_3C and MnN_2C_2 sites in $\text{FeN}_3\text{C}-\text{Mn-1}$ as well as $\text{Pt}(111)$ is the $^*\text{OH}$ desorption with a limiting potential of 0.46 , 0.86 V , and 0.43 V , respectively (Table S6), whereas the RDS of $\text{MnN}_2\text{C}_3-\text{1}$ site is $\text{O}^* \rightarrow \text{OH}^*$ with a limiting potential of 1.04 V . Although the limiting potential of $\text{Pt}(111)$ (0.43 V) is slightly smaller than that of FeN_3C (0.46 V) sites in $\text{FeN}_3\text{C}-\text{Mn-1}$, Fe/Mn HNCS exhibits superior activity than Pt/C with the same metal loading due to its maximum atom-utilization efficiency. Furthermore, the smaller limiting potential of FeN_3C site indicates that FeN_3C site in $\text{FeN}_3\text{C}-\text{Mn-1}$ is the active site for ORR in Fe/Mn -HNCS. This can be attributed to the d-d orbital hybridization between Fe and adjacent Mn atoms. The projected density of states (PDOS) of Fe and Mn atoms in $\text{FeN}_3\text{C}-\text{Mn-1}$ model was computed to analyze the d orbital interactions in the Fe-Mn pairs. As shown in Fig. 4b, the d_{xy} orbitals of Fe

and Mn atoms in $\text{FeN}_3\text{C}-\text{Mn-1}$ model show obvious energy level changes and form a stronger σ -type interaction. While, the d_{xz} / d_{yz} orbitals of Fe and Mn atoms, which are around the Fermi level, show a weak π or δ -type interactions between Fe and Mn atoms. Furthermore, the d_z^2 orbital of Fe atom crosses the Fermi level after incorporation of Mn atoms and overlaps with the d_z^2 orbital of Mn atom. Although the $d_{x^2-y^2}$ orbitals of Fe and Mn atoms also show energy level changes, the hybridization between the $d_{x^2-y^2}$ orbitals of Fe and Mn atoms is negligible. As shown in Fig. S29, the d orbital of Fe and Mn atoms in $\text{FeN}_3\text{C}-\text{Mn-1}$ model show an obvious overlap below the Fermi level over broader energy levels (~ 3.4 to -0.5 eV), which are mainly contributed by the overlap of the d_z^2 and d_{xy} orbitals of Fe and Mn atoms. These results indicate a strong d-d hybridization between Fe and Mn atoms in $\text{FeN}_3\text{C}-\text{Mn-1}$ model (Fig. 4c), which can optimize the electron structure of the Fe and Mn active sites in Fe/Mn -HNCS and facilitate the ORR performance [49–51]. Given that the RDS of ORR for Fe/Fe - and Fe/Mn -HNCS concerns the $^*\text{OH}$ desorption on Fe or Mn site, the interaction between the Fe and Mn sites and $^*\text{OH}$ intermediate was further analyzed by COHP (Fig. 4d). The occupancy of the Fe/Mn - $^*\text{OH}$ antibonding state below Fermi level of the $\text{FeN}_2\text{C}_2-\text{1}$ model is smaller than those of the $\text{FeN}_3\text{C}-\text{Mn-1}$ model, revealing the stronger adsorption strength of the $^*\text{OH}$ intermediates on the $\text{FeN}_2\text{C}_2-\text{1}$ model. Quantitatively, the

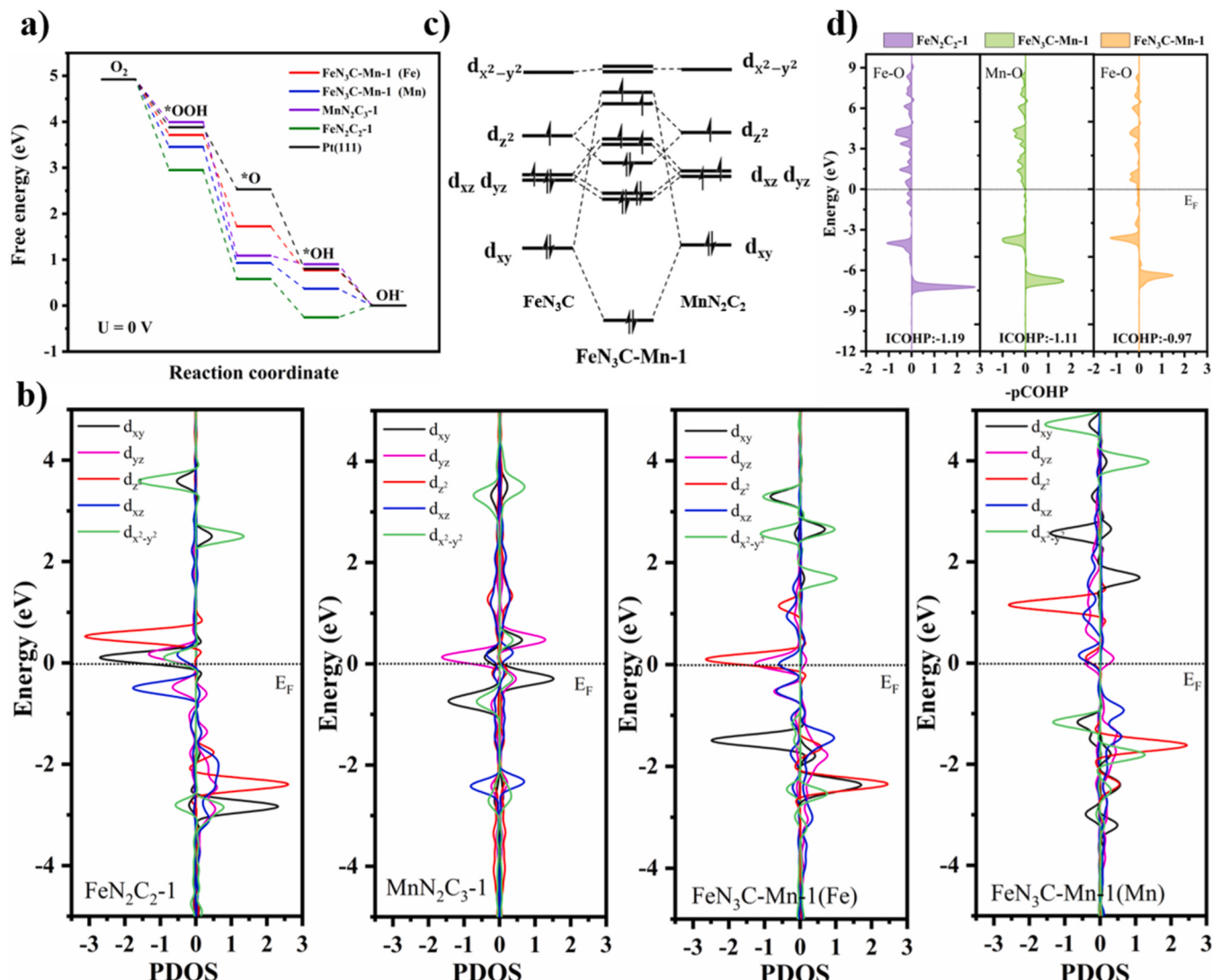


Fig. 4. (a) Free-energy diagram of ORR for different Fe/Mn-centered configurations and $\text{Pt}(111)$. (b) The PDOS of 3d states of Fe and Mn in different Fe/Mn-centered configurations. (c) The d orbital interaction diagrams between Fe and Mn in $\text{FeN}_3\text{C}-\text{Mn-1}$. (d) The $-\text{pCOHP}$ of $\text{Fe}-\text{O}$ / $\text{Mn}-\text{O}$ bond in $\text{FeN}_2\text{C}_2-\text{1}$ and $\text{FeN}_3\text{C}-\text{Mn-1}$ configuration after $^*\text{OH}$ adsorption.

integrated bonding strength of Fe/Mn-*OH were calculated to be -1.19 eV for the $\text{FeN}_2\text{C}_2\text{-}1$ model, which is negative than those of the $\text{FeN}_3\text{C-Mn-}1$ model (-1.11 eV for MnN_2C_2 site and -0.97 eV for FeN_3C site), resulting in the over-strong Fe-*OH bonding strength on the $\text{FeN}_2\text{C}_2\text{-}1$ model. Furthermore, the Bader charge analysis was also performed to quantitatively assess the electron transfer from the Fe or Mn sites to the *OH intermediates. The Bader charge of *OH is more negative on $\text{FeN}_2\text{C}_2\text{-}1$ (-0.451 e) than that on $\text{FeN}_3\text{C-Mn-}1$ (-0.437 e for MnN_2C_2 site and -0.42 e for FeN_3C site), indicating that more electron transfer from $\text{FeN}_2\text{C}_2\text{-}1$ to *OH. The significant electron transfer suggests the strong interaction between *OH with Fe atom on $\text{FeN}_2\text{C}_2\text{-}1$, which is in agreement with the COHP results. Meanwhile, the *OH binding energy on $\text{FeN}_2\text{C}_2\text{-}1$ is -0.26 eV, much lower than those on MnN_2C_2 site (0.37 eV) and FeN_3C site (0.77 eV) in $\text{FeN}_3\text{C-Mn-}1$ model, suggesting a strong adsorption strength of OH* on $\text{FeN}_2\text{C}_2\text{-}1$. Based on the above discussions, it can be inferred that the d-d hybridization between Fe and Mn atoms in $\text{FeN}_3\text{C-Mn-}1$ model can optimize their electronic structures, which were advantageous for *OH desorption, thus boosting the ORR activity of Fe/Mn-HNCS.

4. Conclusions

In summary, a heteronuclear diatomic catalyst Fe/Mn-HNCS with Fe and Mn bimetallic sites embedded into the HNCS matrix was successfully achieved by a two-step anchoring and adsorption method, which was proven by detailed characterization of HAADF-STEM and XAS analysis. Due to the unique dual Fe-Mn configuration, the Fe/Mn-HNCS exhibits excellent ORR performance with E_{onset} of 1.13 V and $E_{1/2}$ of 0.895 V compared to the single atom Fe and Mn catalysts. Theoretical calculations demonstrated that Fe atom in Fe-Mn atomic pair is more active for ORR in Fe/Mn-HNCS, while the existence of an adjacent Mn atom plays an important role in engineering the electronic structures of the Fe site through d-d orbital hybridization. The COHP and Bader charge results further confirmed that the optimized d orbital structure of the Fe site in Fe/Mn-HNCS weakens the over-strong adsorption of *OH, thus resulting in outstanding ORR activity. This work offers a valuable reference for the rational design and construction of atomically dispersed diatomic and even polymetallic central catalysts with superior ORR performance.

CRediT authorship contribution statement

Jun-Kang Li: Conceived the idea, gathered data, analysed, and wrote the manuscript. **Fen-Fen Wang:** Assisted in the data processing. **Yang Zhang:** Conducted the electron tomography measurement. **Rui Wang:** Contributed to the writing modification. **Shu-Na Zhao** and **Shuang-Quan Zang:** Supervised and organized the work. **Shuang-Quan Zang:** Secured funding for this work.

Declaration of Competing Interest

The authors declare no competing financial interest.

Data availability

Data will be made available on request.

Acknowledgements

This work was supported by the National Natural Science Foundation of China (Nos. 21825106, 92061201, 22105175, 52002357, and 22001236), and Postdoctoral Research Grant in Henan Province (No. 202102001).

CRediT authorship contribution statement

Jun-Kang Li: Investigation, Data Curation, Writing-Original draft preparation. **Fen-Fen Wang:** Data Curation. **Yang Zhang:** Formal analysis. **Rui Wang:** Writing-Review&Editing. **Shu-Na Zhao:** Conceptualization, Funding acquisition, Writing-Review&Editing. **Shuang-Quan Zang:** Supervision, Funding acquisition.

Appendix A. Supporting information

Supplementary data associated with this article can be found in the online version at doi:10.1016/j.apcatb.2023.123090.

References

- [1] L. Huang, S. Zaman, X. Tian, Z. Wang, W. Fang, B.Y. Xia, Advanced platinum-based oxygen reduction electrocatalysts for fuel cells, *Acc. Chem. Res.* 54 (2021) 311–322, <https://doi.org/10.1021/acs.accounts.0c00488>.
- [2] X. Qu, Y. Han, Y. Chen, J. Lin, G. Li, J. Yang, Y. Jiang, S. Sun, Stepwise pyrolysis treatment as an efficient strategy to enhance the stability performance of $\text{Fe-N}_x\text{/C}$ electrocatalyst towards oxygen reduction reaction and proton exchange membrane fuel cell, *Appl. Catal. B Environ.* 295 (2021), 120311, <https://doi.org/10.1016/j.apcatb.2021.120311>.
- [3] X. Tian, X.F. Lu, B.Y. Xia, X.W. Lou, Advanced electrocatalysts for the oxygen reduction reaction in energy conversion technologies, *Joule* 4 (2020) 45–68, <https://doi.org/10.1016/j.joule.2019.12.014>.
- [4] S. Zaman, L. Huang, A.I. Douka, H. Yang, B. You, B.Y. Xia, Oxygen reduction electrocatalysts toward practical fuel cells: progress and perspectives, *Angew. Chem. Int. Ed.* 60 (2021) 17832–17852, <https://doi.org/10.1002/anie.202016977>.
- [5] J. Han, H. Bao, J.-Q. Wang, L. Zheng, S. Sun, Z.L. Wang, C. Sun, 3D N-doped ordered mesoporous carbon supported single-atom Fe-N-C catalysts with superior performance for oxygen reduction reaction and zinc-air battery, *Appl. Catal. B Environ.* 280 (2021), 119411, <https://doi.org/10.1016/j.apcatb.2020.119411>.
- [6] K. Zeng, X. Zheng, C. Li, J. Yan, J.H. Tian, C. Jin, P. Strasser, R. Yang, Recent advances in non-noble bifunctional oxygen electrocatalysts toward large-scale production, *Adv. Funct. Mater.* 30 (2020) 2000503, <https://doi.org/10.1002/adfm.202000503>.
- [7] C.X. Zhao, J.N. Liu, J. Wang, D. Ren, B.Q. Li, Q. Zhang, Recent advances of noble-metal-free bifunctional oxygen reduction and evolution electrocatalysts, *Chem. Soc. Rev.* 50 (2021) 7745–7778, <https://doi.org/10.1039/DICS00135C>.
- [8] W. Li, D. Wang, Y. Zhang, L. Tao, T. Wang, Y. Zou, Y. Wang, R. Chen, S. Wang, Defect engineering for fuel-cell electrocatalysts, *Adv. Mater.* 32 (2020) 1907879, <https://doi.org/10.1002/adma.201907879>.
- [9] J. Zhang, J. Zhang, F. He, Y. Chen, J. Zhu, D. Wang, S. Mu, H.Y. Yang, Defect and doping co-engineered non-metal nanocarbon ORR electrocatalyst, *Nano-Micro Lett.* 13 (2021) 65, <https://doi.org/10.1007/s40820-020-00579-y>.
- [10] T. Zhou, N. Zhang, C. Wu, Y. Xie, Surface/interface nanoengineering for rechargeable Zn-air batteries, *Energy Environ. Sci.* 13 (2020) 1132–1153, <https://doi.org/10.1039/C9EE03634B>.
- [11] C. Wan, X. Duan, Y. Huang, Molecular design of single-atom catalysts for oxygen reduction reaction, *Adv. Energy Mater.* 10 (2020) 1903815, <https://doi.org/10.1002/aenm.201903815>.
- [12] Y. Wang, H. Su, Y. He, L. Li, S. Zhu, H. Shen, P. Xie, X. Fu, G. Zhou, C. Feng, D. Zhao, F. Xiao, X. Zhu, Y. Zeng, M. Shao, S. Chen, G. Wu, J. Zeng, C. Wang, Advanced electrocatalysts with single-metal-atom active sites, *Chem. Rev.* 120 (2020) 12217–12314, <https://doi.org/10.1021/acs.chemrev.0c00594>.
- [13] C.X. Zhao, B.Q. Li, J.N. Liu, Q. Zhang, Intrinsic electrocatalytic activity regulation of M-N-C single-atom catalysts for the oxygen reduction reaction, *Angew. Chem. Int. Ed.* 60 (2021) 4448–4463, <https://doi.org/10.1002/anie.202003917>.
- [14] L. Bai, Z. Duan, X. Wen, R. Si, J. Guan, Atomically dispersed manganese-based catalysts for efficient catalysis of oxygen reduction reaction, *Appl. Catal. B Environ.* 257 (2019), 117930, <https://doi.org/10.1016/j.apcatb.2019.117930>.
- [15] G. Gan, X. Li, L. Wang, S. Fan, J. Mu, P. Wang, G. Chen, Active sites in single-atom $\text{Fe-N}_x\text{-C}$ nanosheets for selective electrochemical dechlorination of 1,2-dichloroethane to ethylene, *ACS Nano* 14 (2020) 9929–9937, <https://doi.org/10.1021/acsnano.0c02783>.
- [16] J. Liang, Q. Song, J. Wu, Q. Lei, J. Li, W. Zhang, Z. Huang, T. Kang, H. Xu, P. Wang, X. Zhou, P.K. Wong, H. Li, X. Meng, Z. Jiang, C.S. Lee, Anchoring copper single atoms on porous boron nitride nanofiber to boost selective reduction of nitroaromatics, *ACS Nano* 16 (2022) 4152–4161, <https://doi.org/10.1021/acsnano.1c10003>.
- [17] X. Hai, S. Xi, S. Mitchell, K. Harrath, H. Xu, D.F. Akl, D. Kong, J. Li, Z. Li, T. Sun, H. Yang, Y. Cui, C. Su, X. Zhao, J. Li, J. Perez-Ramirez, J. Lu, Scalable two-step annealing method for preparing ultra-high-density single-atom catalyst libraries, *Nat. Nanotechnol.* 17 (2022) 174–181, <https://doi.org/10.1038/s41565-021-01022-y>.
- [18] J. Li, M. Chen, D.A. Cullen, S. Hwang, M. Wang, B. Li, K. Liu, S. Karakalos, M. Lucero, H. Zhang, C. Lei, H. Xu, G.E. Sterbinsky, Z. Feng, D. Su, K.L. More, G. Wang, Z. Wang, G. Wu, Atomically dispersed manganese catalysts for oxygen reduction in proton-exchange membrane fuel cells, *Nat. Catal.* 1 (2018) 935–945, <https://doi.org/10.1038/s41929-018-0164-8>.

- [19] H. Yin, P. Yuan, B.-A. Lu, H. Xia, K. Guo, G. Yang, G. Qu, D. Xue, Y. Hu, J. Cheng, S. Mu, J.-N. Zhang, Phosphorus-driven electron delocalization on edge-type Fe_N₄ active sites for oxygen reduction in acid medium, *ACS Catal.* 11 (2021) 12754–12762, <https://doi.org/10.1021/acscatal.1c02259>.
- [20] J. Yu, J. Li, C.-Y. Xu, Q. Li, Q. Liu, J. Liu, R. Chen, J. Zhu, J. Wang, Modulating the d-band centers by coordination environment regulation of single-atom Ni on porous carbon fibers for overall water splitting, *Nano Energy* 98 (2022), 107266, <https://doi.org/10.1016/j.nanoen.2022.107266>.
- [21] J. Kim, S.J. Kim, E. Jung, D.H. Mok, V.K. Paidu, J. Lee, H.S. Lee, Y. Jeoun, W. Ko, H. Shin, B.H. Lee, S.Y. Kim, H. Kim, J.H. Kim, S.P. Cho, K.S. Lee, S. Back, S.H. Yu, Y.E. Sung, T. Hyeon, Atomic structure modification of Fe-N-C catalysts via morphology engineering of graphene for enhanced conversion kinetics of lithium-sulfur batteries, *Adv. Funct. Mater.* 32 (2022) 2110857, <https://doi.org/10.1002/adfm.202110857>.
- [22] J. Yang, W. Li, D. Wang, Y. Li, Electronic metal-support interaction of single-atom catalysts and applications in electrocatalysis, *Adv. Mater.* 32 (2020) 2003300, <https://doi.org/10.1002/adma.202003300>.
- [23] Q. He, Y. Zhou, H. Shou, X. Wang, P. Zhang, W. Xu, S. Qiao, C. Wu, H. Liu, D. Liu, S. Chen, R. Long, Z. Oi, X. Wu, L. Song, Synergic reaction kinetics over adjacent ruthenium sites for superb hydrogen generation in alkaline media, *Adv. Mater.* 34 (2022) 2110604, <https://doi.org/10.1002/adma.202110604>.
- [24] Z. Qiao, C. Wang, C. Li, Y. Zeng, S. Hwang, B. Li, S. Karakalos, J. Park, A.J. Kropf, E.C. Wegener, Q. Gong, H. Xu, G. Wang, D.J. Myers, J. Xie, J.S. Spendelow, G. Wu, Atomically dispersed single iron sites for promoting Pt and Pt₃Co fuel cell catalysts: performance and durability improvements, *Energy Environ. Sci.* 14 (2021) 4948, <https://doi.org/10.1039/DIEE01675J>.
- [25] F. Xiao, Q. Wang, G.-L. Xu, X. Qin, I. Hwang, C.-J. Sun, M. Liu, W. Hua, H.-w Wu, S. Zhu, J.-C. Li, J.-G. Wang, Y. Zhu, D. Wu, Z. Wei, M. Gu, K. Amine, M. Shao, Atomically dispersed Pt and Fe sites and Pt-Fe nanoparticles for durable proton exchange membrane fuel cells, *Nat. Catal.* 5 (2022) 503–512, <https://doi.org/10.1038/s41929-022-00796-1>.
- [26] S.N. Zhao, J.K. Li, R. Wang, J. Cai, S.Q. Zang, Electronically and geometrically modified single-atom Fe sites by adjacent Fe nanoparticles for enhanced oxygen reduction, *Adv. Mater.* 34 (2022) 2107291, <https://doi.org/10.1002/adma.202107291>.
- [27] Z. Li, L. Wei, W.-J. Jiang, Z. Hu, H. Luo, W. Zhao, T. Xu, W. Wu, M. Wu, J.-S. Hu, Chemical state of surrounding iron species affects the activity of Fe-N_x for electrocatalytic oxygen reduction, *Appl. Catal. B Environ.* 251 (2019) 240–246, <https://doi.org/10.1016/j.apcatb.2019.03.046>.
- [28] N.K. Wagh, D.H. Kim, S.H. Kim, S.S. Shinde, J.H. Lee, Heuristic iron-cobalt-mediated robust pH-universal oxygen bifunctional lusters for reversible aqueous and flexible solid-state Zn-air cells, *ACS Nano* 15 (2021) 14683–14696, <https://doi.org/10.1021/acsnano.1c04471>.
- [29] L. Huang, J. Chen, L. Gan, J. Wang, S. Dong, Single-atom nanozymes, *Sci. Adv.* 5 (2019) eaav5490, <https://www.science.org/doi/10.1126/sciadv.aav5490>.
- [30] K.M. Zhao, S. Liu, Y.Y. Li, X. Wei, G. Ye, W. Zhu, Y. Su, J. Wang, H. Liu, Z. He, Z. Y. Zhou, S.G. Sun, Insight into the mechanism of axial ligands regulating the catalytic activity of Fe-N₄ sites for oxygen reduction reaction, *Adv. Energy Mater.* 12 (2022) 2103588, <https://doi.org/10.1002/aenm.202103588>.
- [31] C. Jia, X. Tan, Y. Zhao, W. Ren, Y. Li, Z. Su, S.C. Smith, C. Zhao, Sulfur-dopant-promoted electroreduction of CO₂ over coordinatively unsaturated Ni-N₂ moieties, *Angew. Chem. Int. Ed.* 60 (2021) 23342–23348, <https://doi.org/10.1002/anie.202109373>.
- [32] K. Yuan, D. Lutzenkirchen-Hecht, L. Li, L. Shuai, Y. Li, R. Cao, M. Qiu, X. Zhuang, M.K.H. Leung, Y. Chen, U. Scherf, Boosting oxygen reduction of single iron active sites via geometric and electronic engineering: nitrogen and phosphorus dual coordination, *J. Am. Chem. Soc.* 142 (2020) 2404–2412, <https://doi.org/10.1021/jacs.9b11852>.
- [33] T. Cui, Y.P. Wang, T. Ye, J. Wu, Z. Chen, J. Li, Y. Lei, D. Wang, Y. Li, Engineering dual single-atom sites on 2D ultrathin N-doped carbon nanosheets attaining ultra-low-temperature zinc-air battery, *Angew. Chem. Int. Ed.* 61 (2022), e202115219, <https://doi.org/10.1002/anie.202115219>.
- [34] Q. An, J. Jiang, W. Cheng, H. Su, Y. Jiang, Q. Liu, Recent advances in dual-atom site catalysts for efficient oxygen and carbon dioxide electrocatalysis, *Small Methods* 6 (2022) 2200408, <https://doi.org/10.1002/smtd.202200408>.
- [35] G. Yang, J. Zhu, P. Yuan, Y. Hu, G. Qu, B.A. Lu, X. Xue, H. Yin, W. Cheng, J. Cheng, W. Xu, J. Li, J. Hu, S. Mu, J.N. Zhang, Regulating Fe-spin state by atomically dispersed Mn-N in Fe-N-C catalysts with high oxygen reduction activity, *Nat. Commun.* 12 (2021) 1734, <https://doi.org/10.1038/s41467-021-21919-5>.
- [36] N. Zhang, T. Zhou, J. Ge, Y. Lin, Z. Du, C. a Zhong, W. Wang, Q. Jiao, R. Yuan, Y. Tian, W. Chu, C. Wu, Y. Xie, High-density planar-like Fe₂N₆ structure catalyzes efficient oxygen reduction, *Matter* 3 (2020) 509–521, <https://doi.org/10.1016/j.matt.2020.06.026>.
- [37] W. Wan, Y. Zhao, S. Wei, C.A. Triana, J. Li, A. Arcifa, C.S. Allen, R. Cao, G. R. Patzke, Mechanistic insight into the active centers of single/dual-atom Ni/Fe-based oxygen electrocatalysts, *Nat. Commun.* 12 (2021) 5589, <https://doi.org/10.1038/s41467-021-25811-0>.
- [38] Y. Zhang, S. Zhao, J. Feng, S. Song, W. Shi, D. Wang, H. Zhang, Unraveling the physical chemistry and materials science of CeO₂-based nanostructures, *Chem* 7 (2021) 2022–2059, <https://doi.org/10.1016/j.chempr.2021.02.015>.
- [39] A.M. Harzandi, S. Shadman, M. Ha, C.W. Myung, D.Y. Kim, H.J. Park, S. Sultan, W.-S. Noh, W. Lee, P. Thangavel, W.J. Byun, S.-h Lee, J.N. Tiwari, T.J. Shin, J.-H. Park, Z. Lee, J.S. Lee, K.S. Kim, Immiscible bi-metal single-atoms driven synthesis of electrocatalysts having superb mass-activity and durability, *Appl. Catal. B Environ.* 270 (2020), 118896, <https://doi.org/10.1016/j.apcatb.2020.118896>.
- [40] Z. Li, H. He, H. Cao, S. Sun, W. Diao, D. Gao, P. Lu, S. Zhang, Z. Guo, M. Li, R. Liu, D. Ren, C. Liu, Y. Zhang, Z. Yang, J. Jiang, G. Zhang, Atomic Co/Ni dual sites and Co/Ni alloy nanoparticles in N-doped porous Janus-like carbon frameworks for bifunctional oxygen electrocatalysis, *Appl. Catal. B Environ.* 240 (2019) 112–121, <https://doi.org/10.1016/j.apcatb.2018.08.074>.
- [41] H. Jiang, J. Gu, X. Zheng, M. Liu, X. Qiu, L. Wang, W. Li, Z. Chen, X. Ji, J. Li, Defect-rich and ultrathin N doped carbon nanosheets as advanced trifunctional metal-free electrocatalysts for the ORR, OER and HER, *Energy Environ. Sci.* 12 (2019) 322–333, <https://doi.org/10.1039/C8EE03276A>.
- [42] B.H. Lee, S. Park, M. Kim, A.K. Sinha, S.C. Lee, E. Jung, W.J. Chang, K.S. Lee, J. H. Kim, S.P. Cho, H. Kim, K.T. Nam, T. Hyeon, Reversible and cooperative photoactivation of single-atom Cu/TiO₂ photocatalysts, *Nat. Mater.* 18 (2019) 620–626, <https://doi.org/10.1038/s41563-019-0344-1>.
- [43] A. Kumar, V.Q. Bui, J. Lee, L. Wang, A.R. Jadhav, X. Liu, X. Shao, Y. Liu, J. Yu, Y. Hwang, H.T.D. Bui, S. Ajmal, M.G. Kim, S.G. Kim, G.S. Park, Y. Kawazoe, H. Lee, Moving beyond bimetallic-alloy to single-atom dimer atomic-interface for all-pH hydrogen evolution, *Nat. Commun.* 12 (2021) 6766, <https://doi.org/10.1038/s41467-021-27145-3>.
- [44] Y.S. Wei, L. Sun, M. Wang, J. Hong, L. Zou, H. Liu, Y. Wang, M. Zhang, Z. Liu, Y. Li, S. Horike, K. Suenaga, Q. Xu, Fabricating dual-atom iron catalysts for efficient oxygen evolution reaction: heteroatom modulator approach, *Angew. Chem. Int. Ed.* 59 (2020) 16013–16022, <https://doi.org/10.1002/anie.202007221>.
- [45] X. Qu, Y. Han, Y. Chen, J. Lin, G. Li, J. Yang, Y. Jiang, S. Sun, Stepwise pyrolysis treatment as an efficient strategy to enhance the stability performance of Fe-N_x/C electrocatalyst towards oxygen reduction reaction and proton exchange membrane fuel cell, *Appl. Catal. B Environ.* 295 (2021), 120311, <https://doi.org/10.1016/j.apcatb.2021.120311>.
- [46] W. Cheng, P. Yuan, Z. Lv, Y. Guo, Y. Qiao, X. Xue, X. Liu, W. Bai, K. Wang, Q. Xu, J. Zhang, Boosting defective carbon by anchoring well-defined atomically dispersed metal-N₄ sites for ORR, OER, and Zn-air batteries, *Appl. Catal. B Environ.* 260 (2020), 118198, <https://doi.org/10.1016/j.apcatb.2019.118198>.
- [47] J. Zhu, M. Xiao, D. Ren, R. Gao, X. Liu, Z. Zhang, D. Luo, W. Xing, D. Su, A. Yu, Z. Chen, Quasi-covalently coupled Ni-Cu atomic pair for synergistic electroreduction of CO₂, *J. Am. Chem. Soc.* 144 (2022) 9661–9671, <https://doi.org/10.1021/jacs.2c00937>.
- [48] Y. Li, B. Wei, M. Zhu, J. Chen, Q. Jiang, B. Yang, Y. Hou, L. Lei, Z. Li, R. Zhang, Y. Lu, Synergistic effect of atomically dispersed Ni-Zn pair sites for enhanced CO₂ electroreduction, *Adv. Mater.* 33 (2021) 2102212, <https://doi.org/10.1002/adma.202102212>.
- [49] H. Chen, Q. Wu, Y. Wang, Q. Zhao, X. Ai, Y. Shen, X. Zou, d-sp orbital hybridization: a strategy for activity improvement of transition metal catalysts, *Chem. Commun.* 58 (2022) 7730–7740, <https://doi.org/10.1039/D2CC02299K>.
- [50] W. Zou, R. Lu, X. Liu, G. Xiao, X. Liao, Z. Wang, Y. Zhao, Theoretical insights into dual-atom catalysts for the oxygen reduction reaction: the crucial role of orbital polarization, *J. Mater. Chem. A* 10 (2022) 9150–9160, <https://doi.org/10.1039/D2TA00313A>.
- [51] Z. Han, S. Zhao, J. Xiao, X. Zhong, J. Sheng, W. Lv, Q. Zhang, G. Zhou, H.M. Cheng, Engineering d-p orbital hybridization in single-atom metal-embedded three-dimensional electrodes for Li-S batteries, *Adv. Mater.* 33 (2021) 2105947, <https://doi.org/10.1002/adma.202105947>.